European Journal of Mechanics / B Fluids 119 (2026) 204495

Contents lists available at ScienceDirect

European Journal of Mechanics / B Fluids

journal homepage: www.elsevier.com/locate/ejmflu

On the ground effect in passive control using deflectors at the rear part of an Ahmed body☆

P. Solis *, E. Duran, P. Gutierrez-Castillo, C. del Pino

Universidad de Málaga, Institute for Mechatronics Engineering and Cyber-Physical Systems (IMECH.UMA), Campus de Teatinos, s/n 29071, Málaga, Spain

ARTICLE INFO

Keywords:
Ahmed body
Passive control
Bluff body flow
Automotive aerodynamics

ABSTRACT

Drag measurements were performed over an Ahmed body with a 25-degree slant angle modified with rigid deflectors at the top rear edge. Experiments were conducted on both a wind tunnel and a towing water tank in the range of Reynolds numbers based on the height $Re_H = 30\times10^3 - 170\times10^3$. In the wind tunnel experiments, drag measurements were acquired at two ground clearances: a nominal height, and a larger distance 14 times the nominal one to minimize the ground effect. The inclusion of a deflector with an inclination in the range of $\alpha = [-8°, -4°]$ decreases the drag coefficient by up to 27% over the base case without deflector. Furthermore, an analytical correlation was developed to predict the drag coefficient as a function of Reynolds and deflector angle for each ground clearance. Additional 2D-PIV measurements obtained in the towing tank confirmed that the circulation of the C-vortex is significantly reduced compared to the base case. These results demonstrate that the observed drag reduction is primarily associated with a weakening of the induced wake structures.

1. Introduction

One of the main concerns in the design of all vehicles is reducing fuel or electricity consumption. To this end, the aerodynamic characteristics of the vehicle must be improved, particularly the drag coefficient, as a lower value allows the vehicle to move more efficiently, especially at high speeds [1]. The Ahmed body [2] is commonly used as benchmark model in automotive aerodynamics since it reproduces a basic shape with geometrical relevance to heavy road vehicles [3,4]. Studying this bluff body is of great scientific importance in terms of flow detachment at the vehicle rear, subsequent vortex generation under stable and unstable conditions, and wake-vortex decay in the near field downstream [5,6]. The Ahmed body has been extensively tested experimentally for different inflow conditions mostly at very high Reynolds numbers $Re \sim \mathcal{O}(10^5 - 10^6)$. The experimental studies are complemented with computational simulations tests [4,7] with significative relevance in the validation of the turbulence models used [8–12].

In the original manuscript, the Ahmed body had an angle at the rear (φ) that could be zero (square back) or positive (slanted) [2]. In this first study, the evolution of C_D with φ showed a gradual drag reduction and later an increase, reaching the minimum drag at $\varphi_{min} \approx 12.5°$. However, there is no a unique φ value that clearly minimizes C_D, so there is an φ interval where C_D variations are very subtle, $\varphi_{min} \in [7°, 13°]$. They also found a simultaneous high- and low-drag at $\varphi = 30°$. In general, square-back bodies ($\varphi = 0°$) have a simple, large recirculation wake, resulting in different wake flow characteristics, often experiencing a bistable wake state and different pressure distributions [13–19]. Conversely, slanted Ahmed bodies, and typically in the range $\varphi \in [25°, 30°)$ feature complex, three-dimensional vortex separation on the rear slope, leading to higher, angle-dependent drag [4–7,11,20,21].

For a nominal value of ground clearance and the rear slant angle of this study $\varphi = 25°$, there is a small separation bubble on the slanted surface, along with two longitudinal counter-rotating vortices (C-vortices), and two recirculation bubbles behind the vertical base. Experimental observations regarding the interaction between separation bubble on the slanted surface and C-vortices [5] show that the rear part separation zone appears to be more complex than previously found by Ahmed [2]. In particular, their observations showed that the central detached flow region is not closed but contains two separation foci, which slowly evacuate the fluid above the panel into the wake, see figure 14 in [5].

As mentioned above, the flow patterns at the rear and their relationship with aerodynamic characteristics are of particular engineering interest to reduce the drag coefficient. Therefore, for decades, there have been multiple studies focusing on reducing the drag [15,22,23]. To this end, researchers have been using the square back or slanted Ahmed model to apply different passive [24–26] and active flow control techniques [27–29], or even to achieve better performance by

☆ This article is part of a Special issue entitled: 'SFMC25 Adv. Fluid Mech.' published in European Journal of Mechanics / B Fluids.

* Corresponding author.
E-mail address: pedrosg@uma.es (P. Solis).

https://doi.org/10.1016/j.euromechflu.2026.204495

Available online 28 February 2026

combining these two strategies [15]. Most of these techniques address the significant flow separation that occurs at the rear of a ground vehicle. The aforementioned flow structures are the main causes of the onset of drag sources: separation and recirculation bubbles cause the pressure to drop at the rear, while C-vortices are a source of induced drag [1]. Focusing on passive control, rear flexible flaps [26,30] and solid deflectors [23,27] have been used to reduce drag force in different topologies of Ahmed models.

Although deflectors of various sizes and locations have been tested across a range of incident speeds, there is no information about how the ground effect affects their use. Our work is motivated by this lack of information. A summary of all experimental data for a slanted Ahmed body at a nominal ground clearance with deflectors of different lengths and locations can be found in [23]. However, there are large differences for the same type of deflector at the beginning of the slanted surface of the Ahmed model, with drag reductions ranging from 9% at $\varphi = 25°$ [31] to 25% at $\varphi = 30°$ [3] within the same range of $Re \sim \mathcal{O}(10^5 - 10^6)$. For a slanted Ahmed body of $\varphi = 25°$ and nominal clearance, steady RANS simulations also offered good agreement with experiments [3] for the optimal deflector angle close to $\alpha \simeq -5°$ [32]. This result is in excellent agreement with other experimental evidence showing that the drag dramatically decreases at angles above $\alpha \simeq -5°$ [23]. This α value is equivalent to $\varphi = 5°$, which is close to the minimum drag value φ_{min}. However, the two configurations (with and without deflector) are not the same because (i) the deflector never has a rear length l and (ii) there is a cavity between the deflector underside and the top of the slanted area at the rear.

Additionally to the incoming flow conditions, the influence of the ground clearance is also relevant in the flow behavior. For example, the variation in the nominal ground clearance of a square-back Ahmed body strongly affects the stability of the rear wake. Particularly, the experiment made in the absence of a ground proximity showed how the asymmetries of the front and the rear of the body modify the intensity of the base pressure [17]. Besides, ground effects explain the transition process from a stable wake configuration to a bistable state flow configuration [16], and also how ground proximity produces the onset of random reflectional symmetry breaking [13,14]. All of this evidence suggests that varying the ground clearance from a nominal value to the academic experiment without wall effects could be another key parameter in drag reduction using deflectors for a slanted Ahmed body at null yaw angle. Therefore, this paper addresses how C_D depends not only on the Reynolds number Re and the deflector angle α, but also on the ground clearance δ. We analyzed the Ahmed body for a nominal ground clearance as well as a distance that is 14 times greater than the nominal value. Despite representing an academic experiment, this greater ground clearance, neglecting the ground effect, makes the study relevant to aerial or marine vehicles.

There is limited literature assessing the ground clearance for the slanted Ahmed body, and even fewer studies consider the slanted configuration equipped with rear deflectors at ground clearances different from the original one. For this reason, we will consider in this study rigid deflectors at the junction between the roof and the slant of the Ahmed model for different constant angle values. The study aims to understand the aerodynamic effects of rear solid deflectors on a slanted Ahmed body for different incoming velocities, two ground clearances and deflector angular position. The paper is organized in the as follows. Section 2 describes the two experimental set-ups. Section 3 presents and discusses the results, focusing on base flow validation for different force sensors in Section 3.1, drag reduction after applying passive control in Section 3.2, the effect of ground clearance in Section 3.3, PIV results explaining the wake dynamics in Section 3.4 and discussion in Section 3.5. The main conclusions are drawn in Section 4.

2. Experimental setup

2.1. Model

The experiments were carried out using an Ahmed body with a slant angle of $\varphi = 25°$, modified by installing a rear-mounted fixed deflector (see Fig. 1). The deflector is located at the top rear edge and has half the length of the slant ($l/S = 0.50$). Several fixed deflector configurations were tested, varying the deflector angle α from $-16°$ to $+16°$, where $\alpha = 0°$ corresponds to a horizontal configuration, and positive values indicate that the deflector is pitched upwards with respect to the horizontal. The deflectors and the model were manufactured from resin, with the model scaled to a height of H = 72 mm, maintaining geometric similarity with the original Ahmed body. The model has two interchangeable rear sections: one with the original Ahmed geometry and another with a recessed region in the roof where the deflectors are attached using three countersunk screws flush with the surface. For the comparison between ground effect and no ground effect conditions, the four cylindrical supports from the original model were replaced with a single NACA0012 profile, which connected the model to the force sensor. The experiments, which include force and velocity field measurements, were performed in two different facilities: a wind tunnel and a water towing tank, both located at the Laboratory of Aero-Hydrodynamics of the University of Malaga.

2.2. Wind tunnel

The wind tunnel has a test section with a cross-sectional area of 1 m × 1 m and a length of 4 m, with the force sensor at the center of the test section, featuring a turbulence intensity below 1% under all testing conditions. The operating condition is set by fixing the fan power; in our study, this resulted in freestream velocities that covered Reynolds numbers $Re_H = U_\infty H/\nu$ from 60×10^3 to 170×10^3, where U_∞ is the freestream velocity, H is the height of the model, and ν the fluid kinematic viscosity dependent on temperature. Two experimental configurations were tested in the wind tunnel to measure drag forces with and without ground effect.

On one hand, wind tunnel experiments with ground effect (see Fig. 2a) were tested using a false floor board that was installed to suppress the influence of the boundary layer developing over the tunnel floor. The model was positioned at 175 mm above the tunnel floor, while the false floor was adjusted so that the clearance between the bottom of the Ahmed body and the false floor was $\delta_1 = 12.5$ mm. This clearance corresponds to the nominal ground clearance of the original Ahmed experiments [2] scaled to our model size. The board's leading edge, shaped as a NACA0012 airfoil profile to prevent boundary layer separation, was positioned at a distance of 585 mm from the front of the model.

On the other hand, wind tunnel experiments without ground effect (see Fig. 2b) were conducted using the same mounting arrangement as in the previous case, but without the false floor. As a result, the model clearance relative to the tunnel floor was $\delta_2 = 175$ mm. At this distance, which is 14 times greater than the nominal clearance of the Ahmed experiments, there is no interference with the boundary layer developing over the tunnel floor. This avoids the ground effect.

2.3. Towing tank

Additional tests were conducted in a towing tank with a length of 10 m and a cross-sectional area of 0.5 m × 0.5 m to measure drag forces for smaller Re_H and to obtain velocity fields through 2D-PIV experiments. The model moves at velocity U_∞ suspended upside down within the towing tank, maintaining sufficient clearance from the walls to avoid blockage effects, which remained below 4% (see Fig. 3). The model was attached to the force sensor using the same streamlined NACA0012 profile strut employed in the wind tunnel tests,

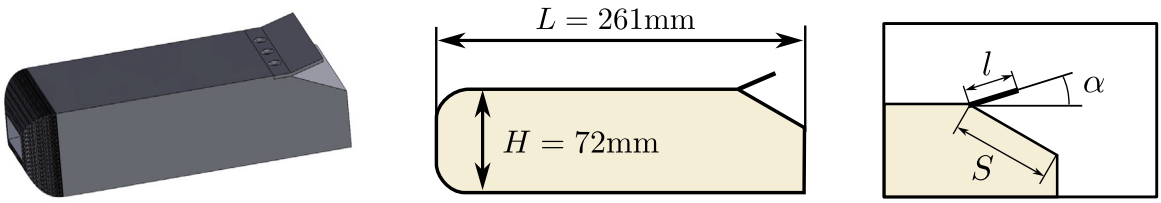

Fig. 1. Three dimensional representation and dimensions of the experimental model: a 1:4 scale version of the original Ahmed body [2] with a slant angle of 25°, modified with a flap at the rear edge. The inset shows a detail of the deflector dimensions and position including the reference for the angle α.

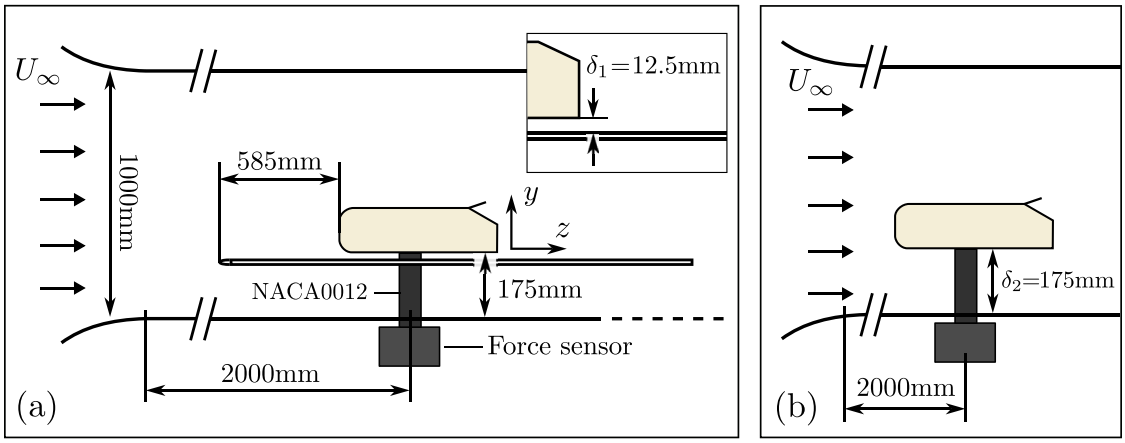

Fig. 2. Experimental setup in the wind tunnel (a) case with ground effect. The inset shows a detail of the ground clearance, (b) case without ground effect.

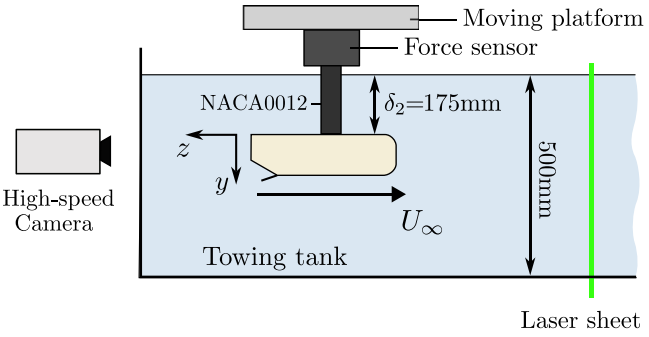

Fig. 3. Experimental setup for the force and PIV measurements in the water towing tank.

thereby minimizing flow interference. The distance between the model underbody and the free surface of the water was $\delta_2 = 175$ mm to replicate the wind tunnel experiments without ground effect. Constant towing speeds were selected, ranging from 0.37 m/s to 0.76 m/s, corresponding to Reynolds numbers from 30×10^3 to 60×10^3. To conduct the 2D-PIV measurements, the laser sheet was set in a fixed, perpendicular position to the towing direction. The high-speed camera recorded the flow on the lee-side of the model in the (x, y)-plane at several locations along the z-coordinate, as shown in Fig. 3.

2.4. Protocol

In summary, three experimental configurations were carried out: one in the wind tunnel with ground effect ($\delta_1 = 0.17H = 12.5$ mm), and two without ground effect ($\delta_2 = 14\delta_1 = 2.43H = 175$ mm), conducted in both the wind tunnel and the towing tank. Force measurements were performed in both facilities and PIV experiments were conducted in the towing tank. To ensure measurement accuracy and repeatability, each experimental condition was tested three times for the force measurements, whereas for the PIV measurements, 50 repetitions were performed to obtain statistically converged averaged velocity fields. Furthermore, temperature and velocity variations were carefully monitored and accounted for in the determination of fluid density and viscosity, ensuring the accuracy and reliability of the Reynolds numbers and drag coefficients obtained. For the wind tunnel experiments, since the operating condition was set by fixing the fan power and the Reynolds number was then calculated from the measured velocity and air temperature, the different experimental configurations were not always tested at exactly the same Reynolds numbers, although the values were comparable.

2.5. Force measurements

Force measurements were conducted in both the wind tunnel and the towing tank using a six-axis force/torque sensor (Schunk FTD-Gamma SI-32-2.5) with an accuracy of ±0.006 N and a sampling frequency of 1 kHz.

For each free-stream velocity U_∞, the force acting on the combined set of the Ahmed body and the NACA0012 profile was measured. Then, the contribution of the NACA0012 profile was measured separately and subtracted from the total force. After this force correction, the non-dimensional drag coefficient C_D was calculated as follows:

$$C_D = \frac{D}{\frac{1}{2}\rho H W U_\infty^2} \tag{1}$$

where D is the corrected drag force after subtracting the support contribution, ρ is the fluid density, U_∞ is the free-stream velocity for wind tunnel tests or the towing velocity for towing tank experiments, H is the model height, and W is the model width. Note that force measurements were repeated at least three times for each experimental condition (except for a limited number of intermediate Reynolds number points in the C_D-Re_H curves) in order to assess consistency. The drag force is computed from the time-averaged drag force signal, and each force graph explicitly displays repeated measurements as separate

markers, which allows for a direct visual assessment of repeatability. Additionally, we have evaluated the time-averaged value over increasing acquisition time intervals to ensure convergence of the mean drag coefficient over time.

2.6. Velocity measurements

For the towing tank experiments, velocity fields were measured using the 2D Particle Image Velocimetry (2D-PIV) technique. For these measurements, a laser sheet was positioned in a fixed position illuminating a plane perpendicular to the axial axis (see Fig. 3). The thin laser sheet (<1 mm thick) was generated using a pair of 1 W green continuous laser sources (Microvec model SM-SEMI-1 W) coupled with cylindrical lenses (6.25 mm focal length). A high-speed monochrome camera (Phantom model CINEMAG-II v611) equipped with a Tamron lens (SP 70–200 mm, f/2.8) was positioned in front of the towing tank, allowing the observation of the model wake evolution. The camera captured images with a resolution of 1280 × 800 px at a frame rate of 400 fps, corresponding to a time interval between consecutive images of $\Delta t = 2.5$ ms. To complete the PIV setup, glass silver-coated spheres of 0.01 mm (HGS-10 from Dantec) were used as tracer particles. These seeding particles are neutrally buoyant in water, thus minimizing their relative motion to the water flow due to gravity and centrifugal accelerations.

For each experiment run, the model moved at $U_\infty = 590$ mm/s, while the measurement plane sheet remained fixed in the laboratory frame. As a result, the recorded image sequence provides snapshots at successive axial positions relative to the model, separated by $\Delta z = U_\infty \Delta t = 1.475 \text{ mm} \approx 0.02H$. Each consecutive image pair yields an instantaneous 2D velocity field, and stacking these planes along the z-axis produces a reconstruction of the entire 3D wake structure, as in [33].

A limitation of this towing-tank configuration is that, in the body-fixed frame, the measurement plane effectively moves downstream at the free-stream velocity. Therefore, within a single run, coherent unsteady features may appear "phase-locked" in the reconstructed wake. To avoid this bias, we repeated the experiment 50 times and computed ensemble-averaged velocity fields, ensuring that the unsteady wake dynamics were sampled at random phases across runs. A convergence study confirmed that the ensemble mean remains essentially unchanged when averaging more than 30 tests.

The instant velocity fields were computed from the images using the DPIVSoft software [34], which is specifically designed for flows with strong rotational motion and implements a double pass PIV method with window deformation. For these measurements, an interrogation window size of 32 × 32 px was used, with an overlap of 79%. The vorticity was numerically derived from the mean velocity field using a second-order finite-difference scheme applied to both velocity components in the (x, y)-plane [35]. Additionally, to quantify and compare the intensity of the C-vortices, we used derived quantities from the mean vorticity field: the wake circulation Γ^+ and the maximum vorticity ω^+ (or Γ^- and ω^- for the clockwise vortex).

The wake circulation was obtained by integrating the vorticity in the desired region:

$$\Gamma^+(z) = \iint_{\omega H/U_\infty > 0.1} \omega(x, y, z)\, dx\, dy,$$
$$\Gamma^-(z) = \iint_{\omega H/U_\infty < -0.1} \omega(x, y, z)\, dx\, dy, \tag{2}$$

where $\Gamma^\pm$ denotes the total integrated circulation of the C-vortices together with secondary wake structures, for counterclockwise and clockwise rotation, respectively. Regions with $|\omega H/U_\infty| \le 0.1$ were excluded from the integration to remove low-vorticity background noise.

The maximum vorticity in each (x, y)-plane is very sensitive to spurious values. Therefore, to obtain a robust measure of vortex intensity, we define ω^+ (and ω^-) as the mean of the highest (or most negative) vorticity samples in each plane as follows:

$$\omega^+(z) = \frac{1}{K} \sum_{(x,y,z)\in P^+} \omega(x, y, z), \qquad \omega^-(z) = \frac{1}{K} \sum_{(x,y,z)\in P^-} \omega(x, y, z), \tag{3}$$

where $P^\pm$ denotes the set of points in the upper and lower 1% percentile of the vorticity values in each (x, y)-plane, respectively, and K denotes the number of points in those sets.

The coordinates $(x_v^\pm,\ y_v^\pm)$ of the C-vortices at each axial distance were estimated as the vorticity-weighted centroids of the region of highest (or most negative) vorticity:

$$x_v^\pm(z) = \frac{\iint_{\Omega^\pm(z)} x\, \omega(x, y, z)\, dx\, dy}{\iint_{\Omega^\pm(z)} \omega(x, y, z)\, dx\, dy}, \qquad y_v^\pm(z) = \frac{\iint_{\Omega^\pm(z)} y\, \omega(x, y, z)\, dx\, dy}{\iint_{\Omega^\pm(z)} \omega(x, y, z)\, dx\, dy}, \tag{4}$$

where the region $\Omega^\pm(z)$ was defined as

$$\Omega^+(z) = \{(x, y) : \omega H/U_\infty \ge 2\}, \qquad \Omega^-(z) = \{(x, y) : \omega H/U_\infty \le -2\}.$$

3. Results

3.1. Validation

Before conducting the experiments involving the novel configurations of the Ahmed body with deflectors, the overall experimental setup was validated to ensure the reliability of both the wind tunnel and towing-tank measurements. The validation procedure was first performed for the wind tunnel setup, including the force sensors and mounting system. For this purpose, measurements were carried out using the base case configuration with the nominal clearance, δ_1, and the resulting drag coefficient was compared with the published data of Bello et al. [4] over a wide range of Reynolds numbers (see Fig. 4a). The comparison shows very good agreement, confirming the accuracy of our experimental methodology and the proper operation of the measurement system.

Due to the limited amount of data available in the literature regarding the drag coefficient without ground effect, the towing tank measurements at δ_2 were validated by comparing them with the wind tunnel results obtained at the same ground clearance, for the two configurations used for the PIV measurements. As shown in Fig. 4b, the towing tank and wind tunnel results overlap and exhibit the same trend, confirming the consistency between the two experimental methodologies. In this regard, it should be emphasized that Ahmed body is fixed in the wind tunnel, as shown in Fig. 2b. However, the towing tank forces the model to move at velocity U_∞ in a steady (non-turbulent) flow upstream, as shown in Fig. 3.

3.2. Effect of deflector angle and Reynolds number on drag coefficient at nominal ground clearance, δ_1

This study aims to minimize drag by using deflectors on flows with Reynolds numbers of the order of 10^5. The main questions are to determine which deflector configuration minimizes the drag, what the maximum possible drag reduction is, and whether changing the Reynolds number affects these two parameters. To address these questions, we analyze the drag behavior for a wide range of α and Re_H.

Fig. 5a shows the variation of C_D with Re_H for several α values. First, it is evident that the deflector configurations affect the value of C_D decreasing it for a certain α range, being $\alpha = -8°$ the case with the lowest C_D. Second, all deflector configurations follow the same decaying trend when increasing Re_H, whereas the base case exhibits a different behavior from $Re_H = 10^5$ onwards. As all the deflector configurations exhibit similar trends, the values of α that most improve

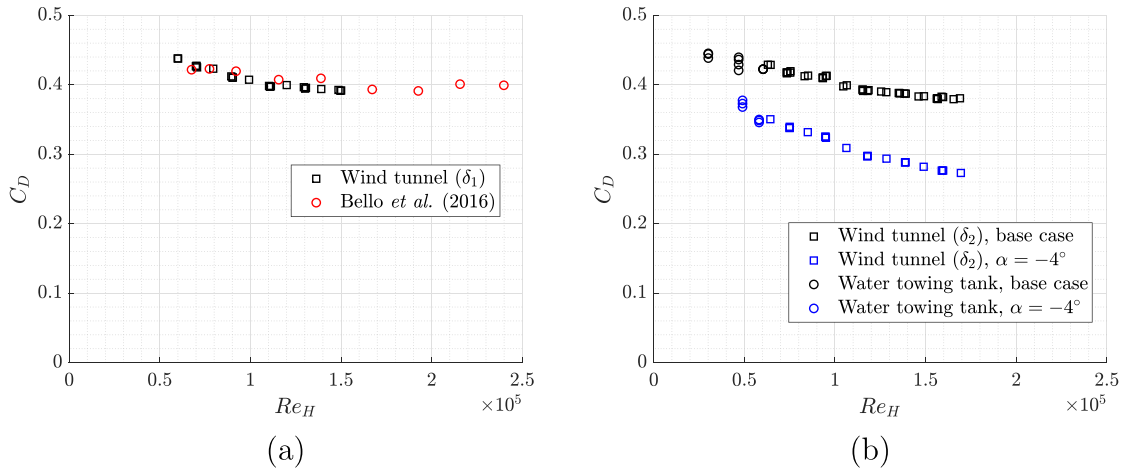

Fig. 4. Drag coefficient (C_D) versus Re_H for the base case model. (a) Wind tunnel measurements at the nominal ground clearance, δ_1, together with the results of Bello et al. [4]. (b) Wind tunnel and towing tank measurements at δ_2.

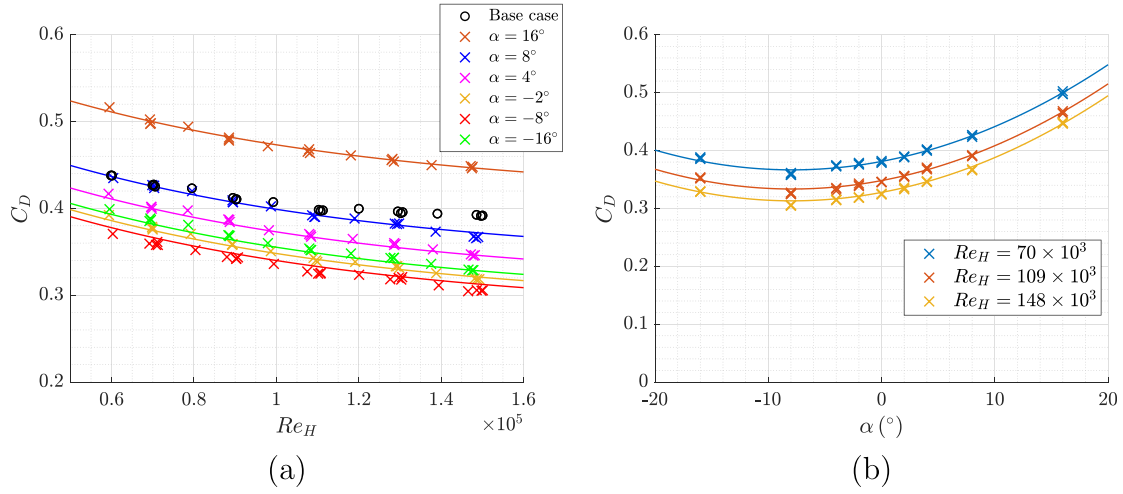

Fig. 5. Drag coefficient for δ_1 ground clearance. Comparison between the experimental data and the values predicted by the proposed formulation. (a) C_D versus Re_H for the base case and six deflector configurations. (b) C_D versus α for three Reynolds numbers.

the aerodynamic behavior of the Ahmed body remain consistent across all Re_H.

Fig. 5b displays C_D variation versus α for three different Re_H values for a closer inspection of the α influence on C_D. Each Re_H series displays the same overall shape and distribution, exhibiting a similar quadratic variation around a α_{opt} independent of Re_H. That minimum C_D among the tested cases occurs at $\alpha = -8°$, followed by $\alpha = -4°$. Therefore, the optimal deflector angle at δ_1 lies around these values.

Based on these observations, a formulation is proposed to estimate the drag coefficient by decoupling the effects of the deflector angle α and the Reynolds number Re_H:

$$C_D(\alpha, Re_H) = C_{D,p}(\alpha) + C_{D,f}(Re_H). \tag{5}$$

This expression separates the total drag coefficient into two independent contributions: a pressure (or form) drag component, $C_{D,p}$, that depends only on the deflector angle, and a viscous friction component that varies with the Reynolds number. This formulation is consistent with the pressure drag being nearly independent of Reynolds for bluff bodies once the flow is fully separated, whereas it can vary significantly with changes in body shape [36]. In our case, variations in α modify the slant and rear flow topology, thus altering the form drag. Conversely, the viscous contribution is only weakly affected by α, but it decreases slightly with increasing Reynolds number due to the thinner boundary layer that develops over the model surface. Accordingly to this decoupled formulation and the previous observations, the pressure drag term is expressed as a quadratic function of α:

$$C_{D,p}(\alpha) = c_0 + c_1(\alpha - \alpha_{\text{opt}})^2, \tag{6}$$

where α_{opt} represents the deflector angle that minimizes drag, c_0 corresponds to the pressure drag contribution of the optimum deflector angle, and c_1 accounts for the sensitivity of drag to variations in the deflector angle.

The friction drag, which depends only on the Reynolds number is defined as:

$$C_{D,f}(Re_H) = c_2\, e^{-Re_H/(10^6\, k)} \tag{7}$$

where c_2 denotes the maximum friction contribution, corresponding to the low Reynolds number limit, and k is a decay constant that determines how rapidly the viscous effects diminish as Re_H increases. The $C_{D,f}$ proposed approximation is consistent with the general structure of the correlation proposed by Bello et al. [4] for the Ahmed body without deflectors which was modeled as an exponential decay function with Re. This exponential behavior reflects the progressive reduction of skin friction drag with increasing Reynolds number due to the thinner boundary layer and lower relative viscous stresses acting on the model surface.

Table 1
Fitted coefficients from experimental data for all deflectors, at nominal ground clearance ($\delta_1 = 0.17H$) and without ground effect ($\delta_2 = 14\delta_1 = 2.43H$).

	c_0	c_1	α_{opt}	c_2	k
δ_1	0.28	2.3×10^{-4}	−7.9	0.20	0.082
δ_2	0.23	2.4×10^{-4}	−5.8	0.22	0.114

Once the approximation function type has been selected, the coefficients of the proposed correlation (c_0, α_{opt}, c_1, c_2 and k) are obtained by performing a global least-squares fit of the proposed expression to the set of experimental data corresponding to deflector angles $\alpha = \{-16°, -8°, -4°, -2°, 0°, 2°, 4°, 8°, 16°\}$, ground clearance δ_1, and Reynolds numbers Re_H between 50×10^3 and 150×10^3. The resulting coefficients are listed in the first row of Table 1. These coefficients result in a root-mean-square error of 0.004, demonstrating that the proposed formulation accurately captures the experimental trends with minimal deviation. The quality of the fit is further illustrated in Fig. 5, where the experimental data are shown together with the analytical fit, while Fig. 6 displays a 3D surface of the fitted function $C_D(\alpha, Re_H)$, with the cross-sections shown in Fig. 5 indicated by black solid lines. Furthermore, the fitted parameters indicate that the pressure drag contribution $C_{D,p}$ represents approximately 70% to 90% of the total drag, which is consistent with the proportions reported by Ahmed [2] for similar slant angle configurations, thereby supporting the physical consistency of the proposed decomposition.

From the fitted coefficients, the optimal angle can be estimated as $\alpha_{opt} = -7.9°$ for the nominal ground clearance, δ_1. The geometric modification introduced by the deflector can be compared to the effect of varying the slant angle of the rear surface in Ahmed's original model, while not being geometrically identical. In fact, the optimal deflector configuration identified here produces a qualitatively similar effect to that of Ahmed's optimal geometry.

To illustrate this phenomenon, Fig. 7 represents C_D vs. α for the current study with relatively long deflectors ($l/S = 0.50$) together with the original Ahmed study [2] when varying the slant angle φ. Note that the geometry of an Ahmed body with a slant angle φ produces a change in slope at the slanted section that is similar to the one produced by a deflector with angle $-\alpha$. This relation between C_D and α is not observed in previous studies with shorter deflectors such as those used in [23,31] ($l/S = 0.09$). In these works, deflectors do not reduce drag until a critical angle is reached, see again Fig. 7. Therefore, the combination between the deflector's length and α is a key parameter to address drag reduction.

These results of the influence of l/S and α on C_D are consistent with the idea that a large part of the drag reduction originates from the weakening of the C-vortices. As previously reported [1,2,5,11,20], this weakening is associated with flow regimes in which the separated shear layer over the slant does not reattach, so that a recirculation bubble on the slanted surface is not formed. For short deflectors, a sufficiently large angle is required to strongly deflect the flow and trigger this regime change. In contrast, with our longer deflectors, a substantial drag reduction is already achieved even at $\alpha = -16°$.

3.3. Comparison between nominal ground clearance, δ_1, and no ground effect conditions, δ_2

The influence of ground clearance on the aerodynamic performance of the Ahmed body with deflectors was analyzed by comparing the results obtained at the nominal ground clearance, δ_1, with those measured under negligible ground effect conditions, δ_2, which is 14 times larger than δ_1. Fig. 8 shows that the variation of C_D with Re_H and α under no ground effect conditions exhibits the same general behavior as that observed for δ_1. Consequently, a fit of the same type as that described for δ_1 was applied for δ_2 measurements, providing good

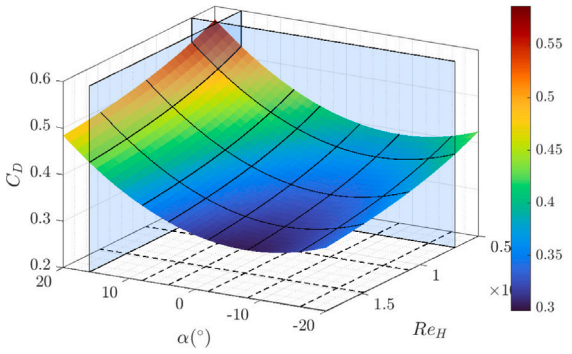

Fig. 6. Three-dimensional surface of the analytical fit $C_D(\alpha, Re_H)$, where the vertical planes represent some of the intersections shown in Fig. 5, and the black lines indicate all the α and Re_H values analyzed in that figure.

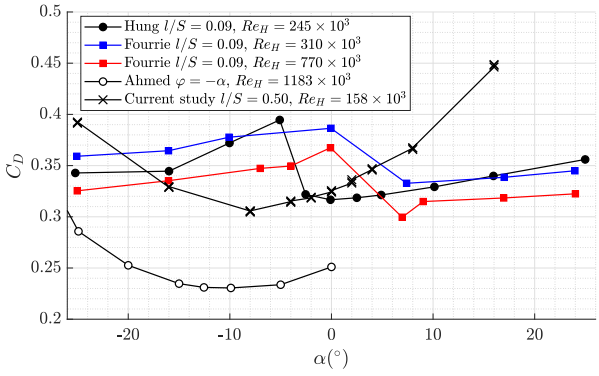

Fig. 7. C_D versus α. Comparison between the present measurements at δ_1, the original Ahmed results (plotted as $\varphi = -\alpha$) [2], and the results with short deflectors ($l/S = 0.09$) from [23,31].

agreement. The analytical correlation accurately reproduces the experimental results for all deflector configurations with a root-mean-square error of less than 0.005. Similar to the δ_1 case, the base case follows a distinct trend from the deflector cases, see Fig. 8a. This difference can be attributed to the geometric disparity between the base model and the deflector configurations, resulting in a different wake flow behavior behind the body.

Even though the variation of C_D with Re_H and α for δ_2 has the same structure than in the δ_1 case, the actual C_D values are different. Fig. 9a presents the variation of C_D with Re_H for the base case and selected deflector angles at both δ_1 and δ_2 to facilitate a direct comparison. For the base case, the influence of ground clearance is very small but the δ_2 cases have a smaller C_D. For the configurations with a deflector, eliminating the ground interaction leads to a significant drag reduction. This drag reduction is mainly produced by the form drag contribution since by removing the influence of the floor, the recirculating flow behind the body is modified. This effect is captured in the analytical fits in variations in the c_0 coefficient, being smaller for the δ_2 case, leading to an overall drag reduction, see Table 1.

Furthermore, the rate of C_D decrease when increasing Re_H is consistently higher for δ_2 than for δ_1 at every α. While the flow over the upper surface of the body remains nearly unchanged before boundary layer separation, the underbody flow is affected by the absence of the floor. This effect modifies the velocity gradients in the underbody area, resulting in a faster decay of the friction drag contribution with increasing Reynolds number, as reflected by the smaller k value, see Table 1.

Another notable difference between the two ground clearances is the shift in the optimal deflector angle, from $\alpha_{opt} = -7.9°$ at δ_1 to

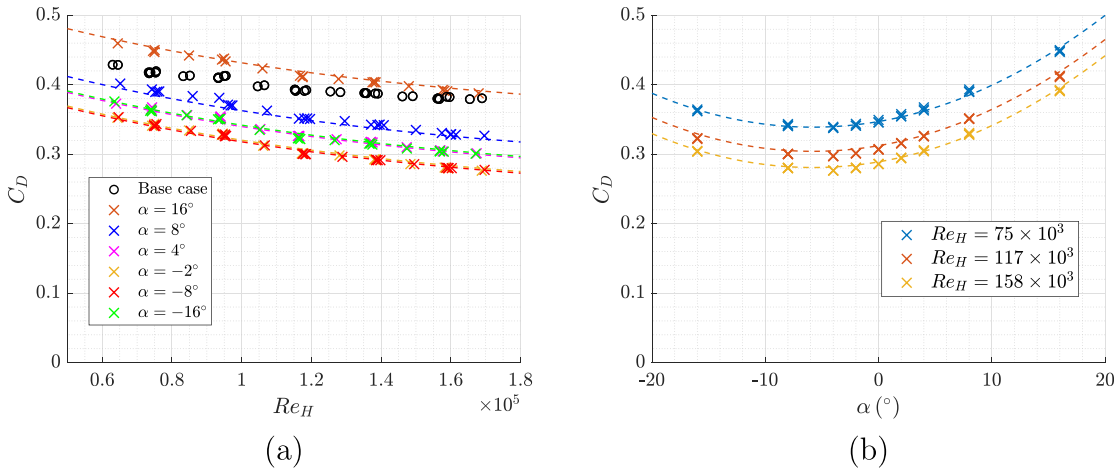

Fig. 8. Drag coefficient for δ_2 ground clearance: comparison between the experimental data and the values predicted by the proposed formulation. (a) C_D versus Re_H for the base case and six deflector configurations. (b) C_D versus α for three Reynolds numbers.

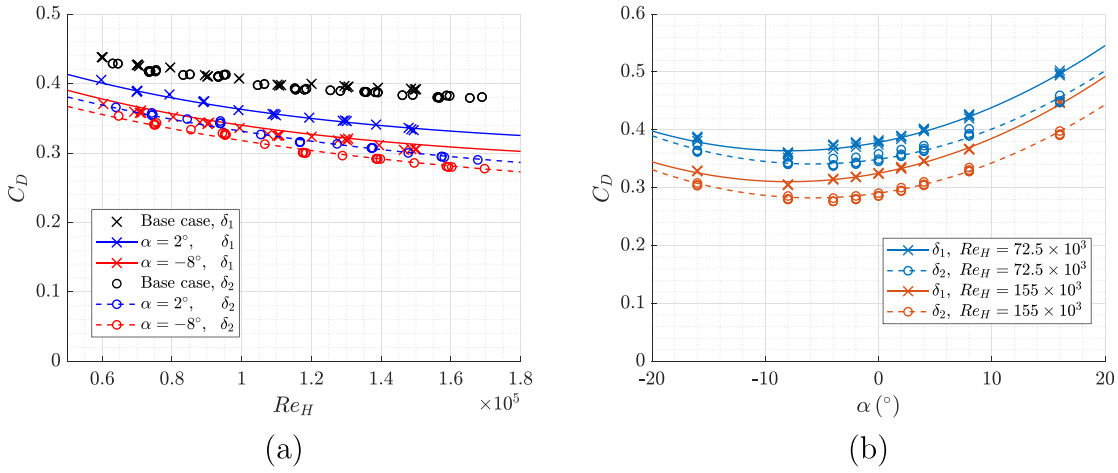

Fig. 9. Comparison of drag coefficient between the nominal ground clearance, δ_1, and the no ground effect clearance, δ_2. Markers represent experimental data, and lines correspond to the values predicted by the proposed formulation. (a) C_D versus Re_H for the base case and two deflector configurations. (b) C_D versus α for two Reynolds numbers.

$\alpha_{opt} = -5.8°$ at δ_2. Fig. 9b shows that, for any given Re_H, the effect of varying δ on C_D is very small for low α, which geometry resembles the base case configuration. The effect of δ on C_D increases monotonically with α up to about a 10% for $\alpha = 16°$.

Table 2 summarizes the drag reduction achieved by all tested deflectors at both ground clearances for two representative Reynolds numbers. In the most favorable case, the deflectors yield a decrease in C_D exceeding 27% with respect to the base case for $Re_H = 155 \times 10^3$. Furthermore, the range of α values producing a substantial drag reduction is relatively broad, spanning more than 10°. This result suggests that deflector-based configurations could be effective even under practical conditions where precise angular positioning is not feasible, as moderate deviations from the optimal angle would not significantly affect performance. Although this study has primarily focused on drag, some lift measurements are also reported for completeness. Fig. 10 presents the variation of C_L with α for several deflector configurations and Reynolds numbers for the two ground clearances studied. The effect of varying δ on the lift is more pronounced than the effect on the C_D. When the model is positioned 14 times farther from the ground, C_L increases by $\Delta C_L \approx 0.20$–0.25, independently of the deflector angle or the Reynolds number. The influence of α is also evident with C_L decreasing nearly linearly as the angle increases. Finally, it can be seen that the Reynolds number has a weak influence on the C_L value.

Table 2
Drag reduction of each deflector configuration relative to the base case. Results are shown for the nominal ground clearance, δ_1, and the no ground effect clearance, δ_2, for two Reynolds numbers. The highest drag reduction for each ground clearance and Reynolds number is highlighted in blue.

	$Re_H = 72.5 \times 10^3$		$Re_H = 155 \times 10^3$	
α (°)	δ_1	δ_2	δ_1	δ_2
−16	9.4 %	13.2 %	16.0 %	20.1 %
−8	15.8 %	18.2 %	22.1 %	26.2 %
−4	12.5 %	19.0 %	19.6 %	27.1 %
−2	11.6 %	18.2 %	18.6 %	26.2 %
0	10.9 %	17.0 %	17.1 %	24.8 %
2	8.7 %	15.1 %	14.6 %	22.5 %
4	5.9 %	13.0 %	11.6 %	19.8 %
8	0.1 %	6.5 %	6.4 %	13.3 %
16	−17.1 %	−7.1 %	−14.2 %	−3.0 %

3.4. PIV results for no ground effect condition, δ_2

To identify the flow features responsible for the observed drag reduction, 2D-PIV measurements were performed in the towing tank for no ground effect clearance δ_2. The experiments were performed over

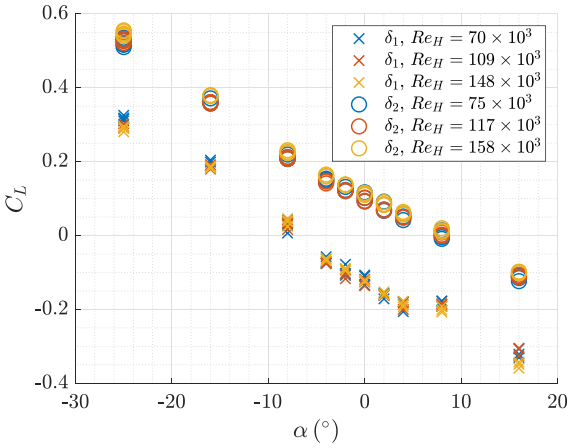

Fig. 10. Lift coefficient versus α for several Re and ground clearances δ_1 and δ_2. The base case is represented at $\alpha = -25°$.

two different models with noticeable drag difference, the base case and $\alpha = -4°$ configuration. Since statistically converged averaged fields of the body wake are necessary, 50 experiments were conducted for each configuration at a constant Reynolds number of 50×10^3 (see again Section 2 for details on the experimental setup). The axial vorticity component was calculated from the mean velocity fields to elucidate the wake dynamics.

Fig. 11 presents the wake vorticity structures obtained from the 2D-PIV measurements for the base case (Fig. 11a–d) and for the configuration with a deflector at $\alpha = -4°$ (Fig. 11e–h). In both cases, the vorticity fields reveal the characteristic counter-rotating longitudinal vortices (C-vortices) generated along the lateral edges of the rear slant, together with secondary vortical structures developing near the model surface. As they move downstream, the C-vortices evolve and adapt to the recirculation bubbles formed behind the vertical base model, defining the near-wake structure [2]. Although the overall topology of the wake is similar in both configurations, there are clear differences in the coherence, strength, and downstream evolution of these vortical structures. To facilitate the detailed description of each case, the z-axis is defined as the streamwise (axial) direction, with its origin at the rear end of the model and positive values extending downstream.

For the base case configuration (Fig. 11a–d), a pair of well-defined C-vortices forms and rolls up rapidly along the sides of the rear slant. After separating from the surface, these vortices open outward and exhibit strong deformation after passing over the vertical basis recirculation bubble, stretching vertically as they are advected downstream until reaching a distance of approximately $z = 2H$. This fact has been reported by other authors, but for the nominal ground clearance configuration [37,38]. Beyond this position $z = 2H$, they gradually concentrate and acquire a nearly circular cross-section, maintaining this structure up to about $z = 5H$. On the slant, and very close to the model surface, a pair of smaller longitudinal counter-rotating vortices develops between the C-vortices [5], each rotating opposite to the vortex on its side and with lower intensity (Fig. 11b). These secondary vortices, which are also visible in the nominal clearance configuration [37,38], dissipate rapidly downstream. Our PIV results depicted in Fig. 11b are also in excellent agreement with those complex structures reported by [5], thus confirming the high quality of the measurements.

For the configuration with a deflector at $\alpha = -4°$ (Fig. 11e–h), the C-vortices still form, but their structure is less concentrated and their overall intensity is lower. Note that, for this reason, a lower vorticity threshold was used in Fig. 11e to represent the 3D isosurface than in Fig. 11a. Since the deflector is located at the beginning of the slant, where the C-vortices originate along its lateral edges, the vortex roll-up process is modified, thereby altering the downstream development of their structure. Moreover, this effect is not limited to the main C-vortices, but also affects the secondary vorticity structures, i.e., the smaller counter-rotating vortices that appear between the C-vortices, which are weaker and dissipate more rapidly downstream (Fig. 11f). As a result, the vorticity field in the deflector configuration appears more diffuse and the overall flow structure is less coherent than in the base case.

To further analyze the streamwise evolution of the C-vortices, two complementary quantities are shown: the circulation $\Gamma^{\pm}$ and the maximum vorticity $\omega^{\pm}$ along the z-axis for both configurations, see Fig. 12a–b. Both $\Gamma^{\pm}$ and $\omega^{\pm}$, computed as defined in Eqs. (2) and (3), exhibit similar overall trends for each configuration reaching a peak shortly after vortex roll-up and then decaying downstream with comparable slopes. However, marked differences arise in terms of intensity and circulation, consistent with the variations observed in the wake structure (Fig. 11). In the base case presented in Fig. 12c the C-vortices are roughly twice as intense as those in the $\alpha = -4°$ configuration depicted in Fig. 12d, with the vorticity peak occurring closer to the model. The smoother evolution in the deflector configuration is physically consistent with its altered flow topology: the presence of the deflector restricts free vortex roll-up along the slant, forcing an interaction between the shear layers of the slant and the deflector. The resulting roll-up produces more elongated and less concentrated vortical structures, leading to lower peak vorticity and a more gradual vortex decay downstream.

Furthermore, the local extreme and inflection points of the $\Gamma^{\pm}$ and $\omega^{\pm}$ evolution along the wake concur with the successive stages of vortex development. In the base case, both quantities exhibit a sharp rise immediately downstream of the rear end (plane A in Fig. 12c), associated with the development of the wake structures originated in the slant. They reach their maximum when the C-vortices pass over the recirculation bubble and stretch (plane B), marking the beginning of their vertical elongation. Once fully stretched, the vortices progressively lose intensity, with a two-stage decay: an initial phase while they remain elongated, followed by a softer decline once they contract and adopt a more circular cross-section (plane C). A secondary inflection in $\Gamma^{\pm}$ appears further downstream (plane D), coinciding with the transition from a region where the vortex core maintains an almost constant size to one where it shrinks progressively, suggesting a redistribution of vorticity within the wake.

In the deflector configuration, the C-vortex evolution is smoother than the base case with some remarkable differences. First, the early slope change identified in the base case before the $\Gamma^{\pm}$ and $\omega^{\pm}$ peaks is absent. In addition, both the peak and the main variation in the decay rate occur further downstream (plane A in Fig. 12d), consistent with the delayed and smoother vortex evolution induced by the deflector. The transition in the decay rate is slightly more pronounced for $\omega^{\pm}$ than for $\Gamma^{\pm}$, appearing at $z \approx 3H$–$4H$, compared with $z \approx 1.5H$–$2.5H$ in the base case. This transition corresponds to a higher dissipation in the wake, as shown in Fig. 12d after plane B.

3.5. Discussion

The 2D-PIV results provide a clear physical explanation for the drag reduction observed in the deflector configurations. The counter-rotating C-vortices are known to play a dominant role in generating pressure drag, as they induce a low-pressure region in the wake immediately behind the body [1,23]. Consequently, any modification of their structure or intensity directly affects the overall form drag. In the present experiments, the inclusion of deflectors weakens these vortices and smooths their development, thereby mitigating the pressure drop at the rear and reducing the total drag. Moreover, the downstream displacement of the vorticity peak, occurring once the vortices stabilize after passing over the vertical basis recirculation bubble, suggests an

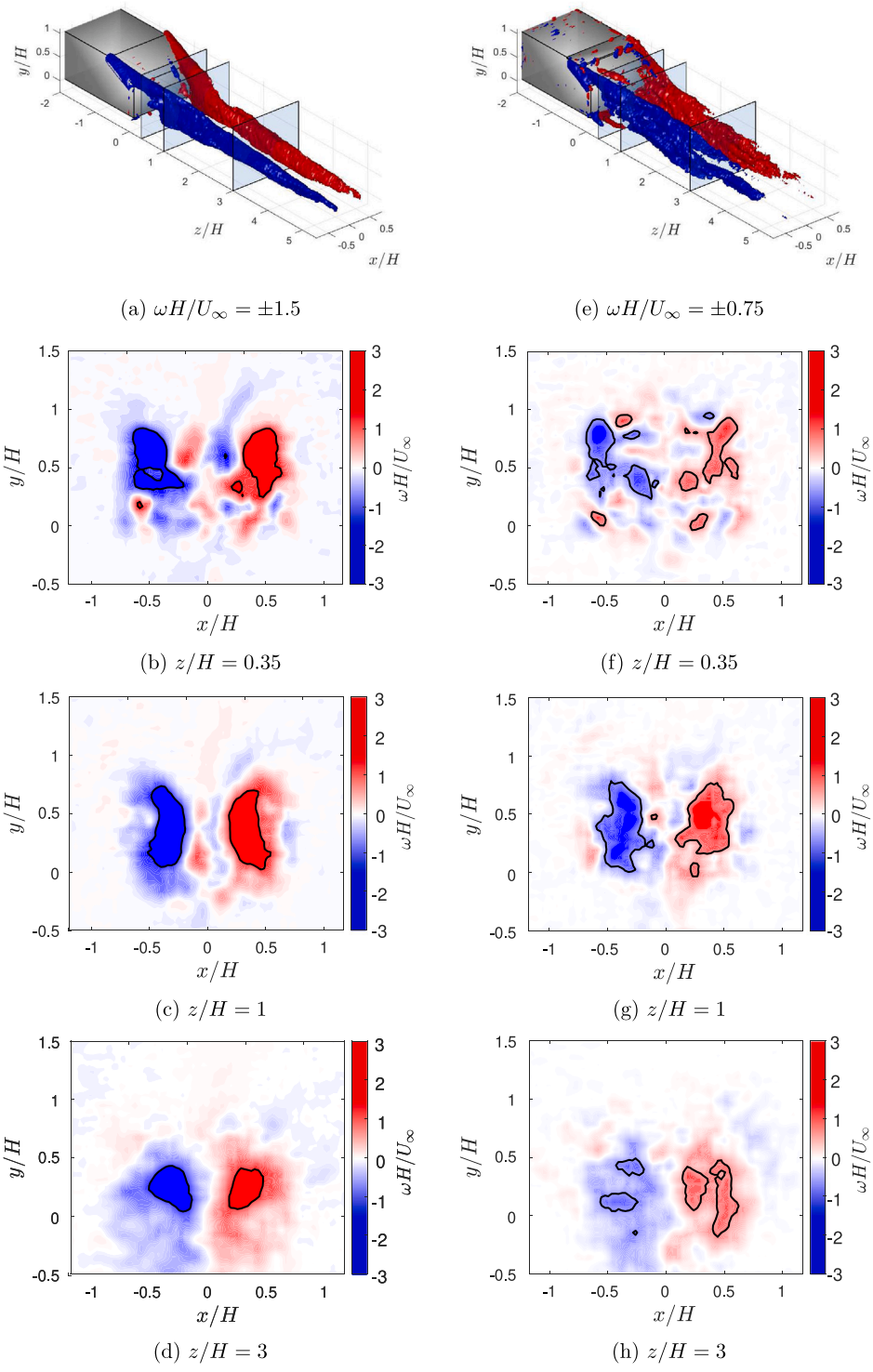

Fig. 11. Wake vorticity structures for the base case (left column) and the $\alpha = -4°$ configuration (right column). Panels (a) and (e) show vorticity isosurfaces at $\omega H/U_\infty = \pm 1.5$ (base case) and ± 0.75 ($\alpha = -4°$). Panels (b–d) and (f–h) present vorticity maps on the three planes indicated in (a) and (e). The isosurface vorticity levels from (a) and (e) are outlined in the vorticity maps by thick black lines.

elongation of this bubble, a phenomenon commonly associated with drag reduction in bluff-body wakes [1,39].

This behavior is consistent with the C_D trends as α varies, shown in Fig. 9b. For small deflector angles, the device remains close to the slant and produces only a small influence on the roll-up along its lateral edges, allowing the formation of strong, concentrated C-vortices that yield high induced drag. Conversely, for positive α values, although the C-vortex generation is significantly disrupted, the deflector introduces new separated flow regions that contribute to an additional drag increase. For some intermediate α values between these two extreme positions, the deflector partially modifies the roll-up process without producing new large scale separations, leading to an effective drag reduction. This analysis also explains the differences observed in previous studies on drag reduction using rear-mounted deflectors at δ_1 [3,31]. In those works, the smaller deflectors employed probably produce weaker

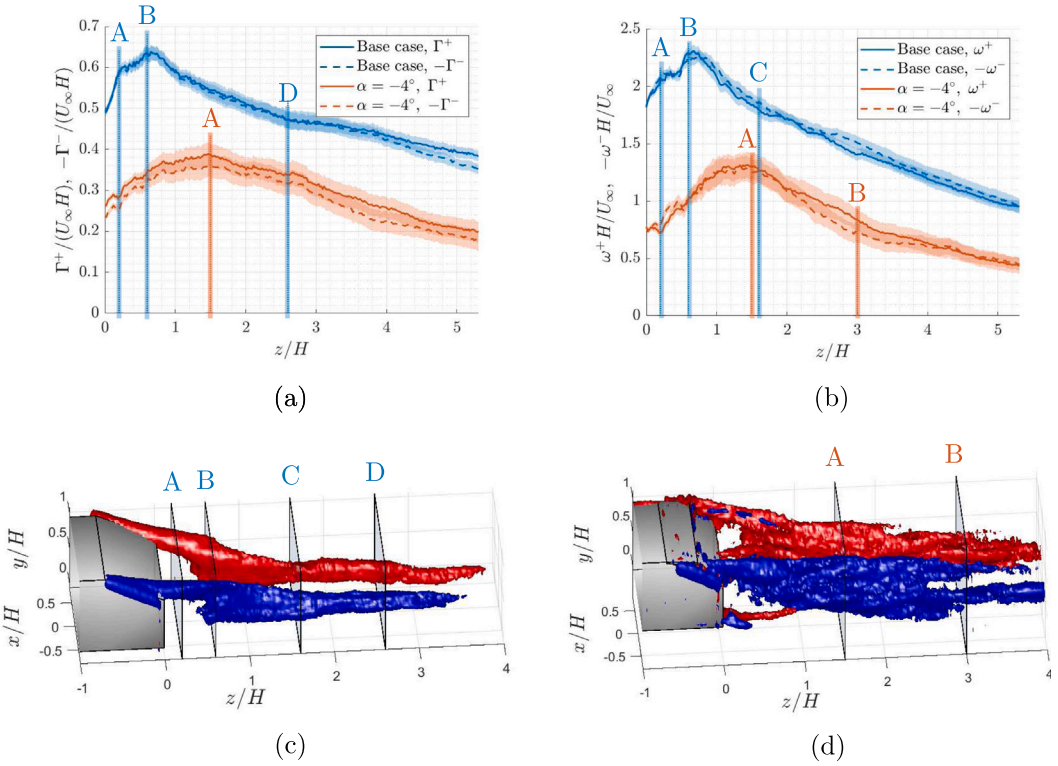

Fig. 12. Circulation and vorticity along the wake for the base case and the $\alpha = -4°$ configuration. (a) Circulation in the (x, y)-plane for both rotation senses, as defined in Eq. (2). (b) Maximum axial vorticity for both rotation senses, as defined in Eq. (3). Blue vertical lines indicate the positions of the planes shown in (c) for the base case wake, and red vertical lines those shown in (d) for the $\alpha = -4°$ configuration. Panels (c) and (d) show vorticity isosurfaces, at $\omega H/U_\infty = \pm 2.2$ for the base case, and at $\omega H/U_\infty = \pm 0.75$ for the deflector configuration. The uncertainty of the quantities $\Gamma^\pm$ and $\omega^\pm$ is represented with translucent bands and it was estimated with the standard deviation of each magnitude evaluated in the instantaneous field using a set of $N = 50$ independent runs and being the integration region ($\pm\omega H/U_\infty > 0.1$, $P^\pm$) obtained from the mean field.. (For interpretation of the references to color in this figure legend, the reader is referred to the web version of this article.)

interference with the roll-up process on the slant, resulting in different flow alteration mechanisms and, consequently, different drag trends.

Concerning the differences observed when ground clearance is altered, our 2D-PIV measurements for the base case without ground effect reveal concentrated C-vortices with very similar structures to those previously reported under ground effect conditions [20,37,38,40]. This resemblance is further illustrated in Fig. 13, which compares our PIV results at δ_2 with published data obtained at nominal ground clearance, showing that the C-vortex structures remain alike for both cases. Due to this similarity in the wake structure, only small differences in form drag are expected. On the other hand, the presence of the ground modifies the underbody flow, generating a boundary layer that alters the local velocity gradients compared with the δ_2 case, thereby affecting the friction drag contribution. However, since the viscous contribution to the total drag is small compared with the form drag for a bluff body, the overall difference between both clearance conditions remains limited, as shown in Fig. 9a.

4. Conclusion

We experimentally determined C_D of an Ahmed body with deflectors having half the length of the slant. We used a wind tunnel and a towing tank for Re_H ranging from 30×10^3 to 170×10^3. The results show that incorporating a deflector with an optimal angle α significantly reduces drag up to 27% in the most favorable configuration. Therefore, including deflectors is a promising way to improve aerodynamic efficiency and the benefits that come with it, such as lower fuel consumption. This drag reduction was observed for both a nominal ground clearance and a higher clearance that minimizes any ground effect, being more pronounced for higher Re_H and greater

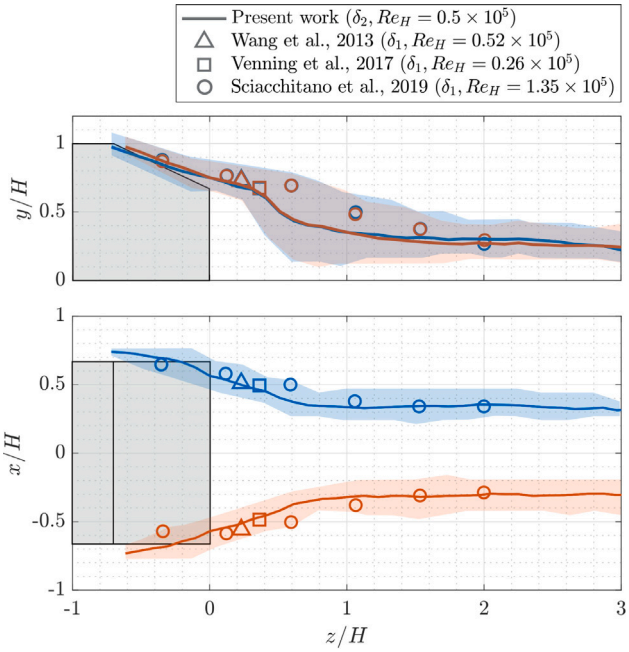

Fig. 13. C-vortices position in the wake for the base case. Comparison between the present PIV results for the no ground effect case (δ_2) and previous PIV measurements from other authors with a slant angle of $\varphi = 25°$ at nominal ground clearance (δ_1) [37,38,40]. The C-vortices positions ($x_v^\pm$, $y_v^\pm$) are computed as defined in Eq. (4), with the regions $\Omega^\pm(z)$ indicated by translucent bands.

ground clearance. Moreover, we have identified an analytical function that approximates C_D for each (Re_H, α) pair for both ground clearances, which will facilitate future design efforts.

Remarkably, for each floor clearance δ, there exists an optimal α for all analyzed Re_H, making the optimal design robust to changes in inflow conditions. Furthermore, the range of α values producing a substantial drag reduction is relatively broad, spanning more than 10°. This result suggests that deflector-based configurations could be effective even under practical conditions where precise angular positioning is not feasible, as moderate deviations from the optimal angle would not significantly affect performance.

2D-PIV measurements reveal that the drag reduction is associated with the attenuation and restructuring of the counter-rotating C-vortices in the vehicle wake. This effect becomes particularly relevant when varying ground clearance, as changes in the wake size and dispersion alter its interaction with the ground and, consequently, the total drag.

In summary, the inclusion of deflectors is clearly beneficial and a crucial part of designs for achieving drag reduction, even with smaller Re than those typically analyzed in most of the bibliography. Possible applications for different vehicle sizes and shapes, both marine and aerial, are numerous, and further investigation into this topic is necessary.

CRediT authorship contribution statement

P. Solis: Writing – original draft, Visualization, Validation, Methodology, Investigation, Formal analysis, Data curation. **E. Duran:** Writing – review & editing, Writing – original draft, Validation, Supervision, Project administration, Methodology, Investigation, Funding acquisition, Formal analysis. **P. Gutierrez-Castillo:** Writing – review & editing, Writing – original draft, Validation, Supervision, Project administration, Methodology, Investigation, Funding acquisition, Formal analysis. **C. del Pino:** Writing – review & editing, Writing – original draft, Validation, Supervision, Methodology, Investigation, Formal analysis, Conceptualization.

Declaration of competing interest

The authors declare that they have no known competing financial interests or personal relationships that could have appeared to influence the work reported in this paper.

Acknowledgments

This work was supported by the Junta de Andalucía ProyExcel_00313 and by the Spanish Government PID2021-124692OA-I00. Also, authors would like to thank students José Antonio Santiago-Galván and Alejandro Bravo Ruiz for their participation in this research work. Finally, we would to thank Prof. Dr. Enrique Sanmiguel-Rojas for his fruitful discussions.

Data availability

Data will be made available on request.

References

[1] H. Choi, J. Lee, H. Park, Aerodynamics of heavy vehicles, Annu. Rev. Fluid Mech. 46 (2014) 441–468, http://dx.doi.org/10.1146/annurev-fluid-011212-140616.

[2] S. Ahmed, G. Ramm, G. Faltin, Some Salient Features of the Time-Averaged Ground Vehicle Wake, SAE aper 840300, 1984, http://dx.doi.org/10.4271/840300.

[3] J.-F. Beaudoin, J.-L. Aider, Drag and lift reduction of a 3D bluff body using flaps, Exp. Fluids 44 (2008) 491–501, http://dx.doi.org/10.1007/s00348-007-0392-1.

[4] F. Bello-Millán, T. Mäkelä, L. Parras, C. del Pino, C. Ferrera, Experimental study on ahmed's body drag coefficient for different yaw angles, J. Wind Eng. Ind. Aerodyn. 157 (2016) 140–144, http://dx.doi.org/10.1016/j.jweia.2016.08.005.

[5] A. Spohn, P. Gilliéron, Flow separations generated by a simplified geometry of an automotive vehicle, in: IUTAM Symposium: Unsteady Separated Flows, 2002, p. 171.

[6] G. Moscato, G. Paolo Romano, Aerodynamic performances and near wake of an Ahmed body under unsteady flow conditions, Exp. Therm. Fluid Sci. 160 (2025) 111285, http://dx.doi.org/10.1016/j.expthermflusci.2024.111285.

[7] A. Thacker, S. Aubrun, A. Leroy, P. Devinant, Effects of suppressing the 3D separation on the rear slant on the flow structures around an Ahmed body, J. Wind Eng. Ind. Aerodyn. 107 (2012) 237–243, http://dx.doi.org/10.1016/j.jweia.2012.04.022.

[8] S. Krajnović, L. Davidson, Flow around a simplified car, Part 1: Large eddy simulation, J. Fluids Eng. 127 (5) (2005) 907–918, http://dx.doi.org/10.1115/1.1989371.

[9] E. Guilmineau, Computational study of flow around a simplified car body, J. Wind Eng. Ind. Aerodyn. 96 (6) (2008) 1207–1217, http://dx.doi.org/10.1016/j.jweia.2007.06.041.

[10] M. Mirzaei, S. Krajnović, B. Basara, Partially-Averaged Navier–Stokes simulations of flows around two different ahmed bodies, Comput. & Fluids 117 (2015) 273–286, http://dx.doi.org/10.1016/j.compfluid.2015.05.010.

[11] E. Guilmineau, G. Deng, A. Leroyer, P. Queutey, M. Visonneau, J. Wackers, Assessment of hybrid RANS-LES formulations for flow simulation around the Ahmed body, Comput. & Fluids 176 (2018) 302–319, http://dx.doi.org/10.1016/j.compfluid.2017.01.005.

[12] W. Zeidan, N. Mazellier, E. Guilmineau, P.-Y. Passaggia, A. Kourta, A near-wake survey of an Ahmed body comparing low- & high-fidelity numerical models with experiments, Eur. J. Mech. B Fluids 101 (2023) 195–208, http://dx.doi.org/10.1016/j.euromechflu.2023.05.002.

[13] M. Grandemange, O. Cadot, M. Gohlke, Reflectional symmetry breaking of the separated flow over three-dimensional bluff bodies, Phys. Rev. E 86 (2012) 035302, http://dx.doi.org/10.1103/PhysRevE.86.035302.

[14] M. Grandemange, M. Gohlke, O. Cadot, Bi-stability in the turbulent wake past parallelepiped bodies with various aspect ratios and wall effects, Phys. Fluids 25 (9) (2013) 095103, http://dx.doi.org/10.1063/1.4820372.

[15] C.-H. Bruneau, E. Creusé, P. Gilliéron, I. Mortazavi, Effect of the vortex dynamics on the drag coefficient of a square back Ahmed body: Application to the flow control, Eur. J. Mech. B Fluids 45 (2014) 1–11, http://dx.doi.org/10.1016/j.euromechflu.2013.11.003.

[16] B. Plumejeau, L. Keirsbulck, S. Delprat, M. Lippert, W. Abassi, Behavior of the square-back Ahmed body global modes at low ground clearance, Phys. Rev. Fluids 5 (2020) 084701, http://dx.doi.org/10.1103/PhysRevFluids.5.084701.

[17] A. Legeai, O. Cadot, On the recirculating flow of three-dimensional asymmetric bluff bodies, Exp. Fluids 61 (12) (2020) 249, http://dx.doi.org/10.1007/s00348-020-03083-6.

[18] Y. Fan, V. Parezanović, O. Cadot, Wake transitions and steady z-instability of an Ahmed body in varying flow conditions, J. Fluid Mech. 942 (2022) A22, http://dx.doi.org/10.1017/jfm.2022.382.

[19] Y. Fan, C. Xia, G. Minelli, S. Sebben, O. Cadot, Recirculating flow structures of a square-back ahmed body at a variable attitude, J. Fluid Mech. 1023 (2025) A30, http://dx.doi.org/10.1017/jfm.2025.10833.

[20] K. Liu, B. Zhang, Y. Zhang, Y. Zhou, Flow structure around a low-drag Ahmed body, J. Fluid Mech. 913 (2021) A21, http://dx.doi.org/10.1017/jfm.2020.1136.

[21] N.A. Siddiqui, M. Agelin-Chaab, Flow features of the Ahmed body at a low Reynolds number, Int. J. Heat Fluid Flow 98 (2022) 109052, http://dx.doi.org/10.1016/j.ijheatfluidflow.2022.109052.

[22] T. Han, D.C. Hammond, C.J. Sagi, Optimization of bluff body for minimum drag in ground proximity, AIAA J. 30 (4) (1992) 882–889, http://dx.doi.org/10.2514/3.11005.

[23] T. The Hung, M. Hijikuro, M. Anyoji, T. Uchida, T. Nakashima, K. Shimizu, Surface flow and aerodynamic drag of Ahmed body with deflectors, Exp. Therm. Fluid Sci. 145 (2023) 110887, http://dx.doi.org/10.1016/j.expthermflusci.2023.110887.

[24] F.F. Buscariolo, G.R. Assi, S.J. Sherwin, Computational study on an Ahmed body equipped with simplified underbody diffuser, J. Wind Eng. Ind. Aerodyn. 209 (2021) 104411, http://dx.doi.org/10.1016/j.jweia.2020.104411.

[25] S.-Y. Cheng, K.-Y. Chin, S. Mansor, A.B. Abd Rahman, Experimental study of yaw angle effect on the aerodynamic characteristics of a road vehicle fitted with a rear spoiler, J. Wind Eng. Ind. Aerodyn. 184 (2019) 305–312, http://dx.doi.org/10.1016/j.jweia.2018.11.033.

[26] J. Camacho-Sánchez, M. Lorite-Díez, J. Jiménez-González, O. Cadot, C. Martínez-Bazán, Experimental study on the effect of adaptive flaps on the aerodynamics of an Ahmed body, Phys. Rev. Fluids 8 (4) (2023) 044605, http://dx.doi.org/10.1103/PhysRevFluids.8.044605.

[27] T. The Hung, M. Hijikuro, M. Anyoji, T. Uchida, T. Nakashima, K. Shimizu, Deflector effect on flow behavior and drag of an Ahmed body under crosswind conditions, J. Wind Eng. Ind. Aerodyn. 231 (2022) 105238, http://dx.doi.org/10.1016/j.jweia.2022.105238.

[28] B. Plumejeau, L. Keirsbulck, J. Basley, M. Lippert, S. Delprat, W. Abassi, Drag mitigation by steady blowing and Coanda effect on a square back Ahmed body, Eur. J. Mech. B Fluids 98 (2023) 80–91, http://dx.doi.org/10.1016/j.euromechflu.2022.11.006.

[29] P. Duy, T. Hung, L. Anh, T. Long, N. Siddiqui, Drag behavior of 25° Ahmed body effect by deflector length and angles, Int. J. Heat Technol. 42 (2024) 1484–1494, http://dx.doi.org/10.18280/ijht.420438.

[30] J. Muñoz-Hervás, M. Lorite-Díez, C. García-Baena, J. Jiménez-González, Experimental investigation of rear flexible flaps interacting with the wake dynamics behind a squareback Ahmed body, J. Fluids Struct. 127 (2024) 104124, http://dx.doi.org/10.1016/j.jfluidstructs.2024.104124.

[31] G. Fourrié, L. Keirsbulck, L. Labraga, Bluff-body drag reduction using a deflector, Exp. Fluids 50 (2011) 385–395, http://dx.doi.org/10.1007/s00348-010-0937-6.

[32] J. Tian, Y. Zhang, H. Zhu, H. Xiao, Aerodynamic drag reduction and flow control of Ahmed body with flaps, Adv. Mech. Eng. 9 (7) (2017) 1687814017711390, http://dx.doi.org/10.1177/1687814017711390.

[33] T.I. Khan, L. Pastur, O. Cadot, V. Parezanović, Equilibrium of fluid fluxes in the wake of a three-dimensional flat-back bluff body, J. Fluid Mech. 997 (2024) A60, http://dx.doi.org/10.1017/jfm.2024.614.

[34] P. Meunier, T. Leweke, Analysis and treatment of errors due to high velocity gradients in particle image velocimetry, Exp. Fluids 35 (2003) 408–421, http://dx.doi.org/10.1007/s00348-003-0673-2.

[35] J.H. García-Ortiz, A. Domínguez-Vázquez, J. Serrano-Aguilera, L. Parras, C. del Pino, A complementary numerical and experimental study of the influence of Reynolds number on theoretical models for wingtip vortices, Comput. & Fluids 180 (2019) 176–189, http://dx.doi.org/10.1016/j.compfluid.2018.12.009.

[36] J.D. Anderson, Fundamentals of Aerodynamics, sixth ed., McGraw-Hill Education, New York, 2017.

[37] A. Sciacchitano, D. Giaquinta, Investigation of the Ahmed body cross-wind flow topology by robotic volumetric PIV, in: C.J. Kähler, R. Hain, S. Scharnowski, T. Fuchs (Eds.), Proceedings of the 13th International Symposium on Particle Image Velocimetry (ISPIV 2019), Universität der Bundeswehr München, 2019, pp. 311–320, http://dx.doi.org/10.18726/2019_3.

[38] X. Wang, Y. Zhou, Y. Pin, T. Chan, Turbulent near wake of an Ahmed vehicle model, Exp. Fluids 54 (4) (2013) 1490, http://dx.doi.org/10.1007/s00348-013-1490-x.

[39] M. Lorite-Díez, J. Jiménez-González, C. Gutiérrez-Montes, C. Martínez-Bazán, Drag reduction of slender blunt-based bodies using optimized rear cavities, J. Fluids Struct. 74 (2017) 158–177, http://dx.doi.org/10.1016/j.jfluidstructs.2017.07.011.

[40] J. Venning, D.L. Jacono, D. Burton, M. Thompson, J. Sheridan, The nature of the vortical structures in the near wake of the Ahmed body, Proc. Inst. Mech. Eng. D: J. Automob. Eng. 231 (9) (2017) 1239–1244, http://dx.doi.org/10.1177/0954407017690683.